Modeled Optimization and Experimental Verification of a Low-Dispersion Source for Long-Haul 2.488-Gbit/s Systems

Stephen M. Gee

Herbert Lage

Chris Park

Kevin A. Williams

Richard V. Penty

Ian H. White

Joseph A. Barnard

This paper describes microwave, laser, and fiber models that were used in the development of the HP LSC2500 2.488-Gbit/s laser diode module. Knowledge of the modeled behavior of the laser diode as a function of the input electrical pulse shape has led to deliberately shaping the input pulse to give the minimum wavelength excursion during direct modulation, and therefore a high yield of low-dispersion-penalty laser diodes. These devices can be successfully used for transmission distances in excess of 200 km.

A s digital modulation speeds increase to meet increasing demands on capacity, and as transmission lengths become longer with the availability of narrow-linewidth sources and optical amplifiers, a requirement for low-dispersion-penalty laser diodes has emerged. ***Dispersion penalty*** is caused by the wavelength dependence of propagation speed in optical fiber, resulting in the different wavelength components of the optical pulse traveling at different speeds along the fiber and arriving at the receiver with variable delay. In extreme cases, optical power generated during one bit period can arrive at the receiver during the adjacent bit period, causing errors, a problem exacerbated in high-frequency systems with short bit periods. Even in truly single-mode laser diodes, when modulated directly by applying an electrical signal to the laser bias, the optical signal can be composed of a range of wavelengths because the wavelength itself is bias dependent, a property known as *laser chirp*. More advanced laser diodes with integral modulation sections are becoming available, but even these have some wavelength modulation caused by optical effects within the diode.

Since the penalty caused by laser chirp is dependent on drive conditions, packaging, and laser chip properties, we have developed a model that can take the input electrical data and predict the electrical signal reaching the laser diode, taking into account package effects. The model then predicts the output optical pulse from the laser based on laser chip parameters. A fiber model is added to predict the optical pulse shape after a known length of fiber.

This model has been used to develop the HP LSC2500, an optically isolated, 1550-nm, 2.488-Gbit/s, distributed feedback (DFB) laser module. The model has helped with the development of both the packaging and the laser chip.

The model was developed jointly by the HP Ipswich Components Operation (ICO), Bristol University, and Barnard Micro-systems Limited. The experimental comparison has been carried out at ICO. Models have been developed for other laser structures such as electroabsorption modulators (EADFB). These models will help with the design of components for higher frequencies (10 Gbits/s).

This paper includes predicted results from the modeling and actual results measured on the finished product. Sections in this paper introduce the microwave model, the laser model, and the fiber model. A description is given of the laser diode. Experimental results compare the measured and predicted microwave s-parameters and also the measured and predicted optical pulses both before and after the fiber. Dispersion penalty measurements are included, showing that directly modulated DFB lasers with low chirp can, in practice, operate over fiber transmission distances in excess of 200 km.

DFB Laser Chip Design

The design of the distributed feedback (DFB) laser diode is based upon ICO's proven ridge waveguide technology. The laser has a strained multiple quantum well active region grown by metalorganic vapor-phase epitaxy and a first-order DFB grating. The front and back facets are antireflection and high-reflection coated, respectively. The chip is mounted with the active region uppermost on a silicon carbide heat sink.

The quarternary material system consisting of combinations of the four elements indium (In), gallium (Ga), arsenic (As) and phosphorus (P) is used for the growth of the epitaxial layers. The number of quantum wells in the active region and the strain—that is, the mismatch of the lattice constant of the quantum wells with respect to the InP substrate—have been optimized for high-speed performance and fast response to changes in drive current. In particular, the shift of the emission wavelength under modulation (chirp) has been minimized to reduce the dispersion penalty in long-haul fiber-optic links. The compressive strain of the quantum wells is compensated by opposite strain in the barriers to avoid any impact of the strain on the reliability of the devices. The thickness of each strained layer is below the critical limit at which relaxation occurs.

Mode selectivity is achieved by a uniform first-order grating with a coupling coefficient of approximately 30 to 40 cm^{-1}. This relatively modest coupling efficiency was chosen to keep the photon density uniform inside the cavity and to prevent distortion of the light-versus-current characteristic. The antireflection and high-reflection coatings are applied to improve the suppression of side modes and to enhance the front-facet efficiency of the devices.

Typical device parameters are summarized in **Table I**. The low internal loss and the high gain of the strained multiple quantum well active region results in average threshold currents of only 16 mA. The front-facet efficiency of 0.35 mW/mA is an excellent achievement for DFB lasers in the 1550-nm wavelength range, where lasers typically suffer from low internal quantum efficiencies. The linewidth is measured under 2.5-Gbit/s modulation with 12% extinction ratio (power in the off state divided by power in the on state) and found to be around 0.4 nm (with the reading taken 30 dB below the peak). This shows the good wavelength stability and therefore low chirp of the device under intensity modulation and proves its suitability for high-speed long-haul data transmission systems. The small broadening of the linewidth under modulation is in agreement with a direct measurement of the chirp.

| Table I		
Laser Diode Parameters		
Parameter	**Symbol**	**Value**
Length	L	350 μm
Threshold Current	I_{th}	16 mA
Front-Facet Efficiency	η	0.35W/A
30-dB Linewidth without Modulation		0.38 nm
30-dB Linewidth with Modulation		0.42 nm

Laser Driver Circuit Model

The 2.488-Gbit/s pulses into the laser diode transmitter package can be generated by a signal generator, which can be either a pseudorandom binary sequence (PRBS) nonreturn-to-zero (NRZ) waveform generator test set or a laser driver chip. The laser driver chip can be based on a fast silicon bipolar technology such as the Hewlett-Packard HP-25 process, or on a GaAs FET technology.

Initially we need to know the frequency range that we should be concerned with. We describe the 2.488-Gbit/s waveform with a 75-ps 10%-to-90% rise time through the use of a Fermi function to define the rising and falling pulse edges. The use of this function, more usually applied in the area of semiconductor device physics, gives a reasonable approximation to the true waveform from real signal generators. We create a 128-bit PRBS waveform and take the fast Fourier transform (FFT) of the waveform to get an idea of the spectral distribution of the energy in the waveform.

A 2.488-Gbit/s signal was obtained from an HP 70841B PRBS signal generator and its spectrum was monitored on an HP 71400 lightwave signal analyzer. **Figure 1a** shows the predicted waveform and **Figure 1b** shows the predicted spectrum. The spectrum agreed well with our predictions. From the spectrum, we see that we should principally be concerned with the energy from very low frequencies up to about 2 GHz.

Figure 1

(a) The predicted 2.488-Gbit/s signal obtained from an HP 70841B PRBS signal generator. (b) The spectrum predicted for the 2.488-Gbit/s signal.
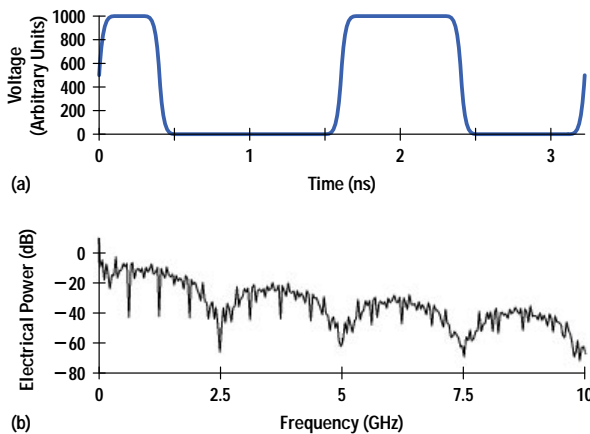
It is important to know the attributes of the driver circuit to account for any multiple reflections between the signal generator and impedance discontinuities in the laser package. If the signal generator is a PRBS test set, then the equivalent circuit for the source is well-approximated by a voltage source in series with a 50-ohm resistance. If a laser driver chip is used, the characterization of the source impedance is more complex, and can be divided into two cases. In the first case, in which we have all the information on the driver circuit (including small-signal and large-signal circuit models), the extraction of a relatively simple circuit describing the source impedance characteristics of the driver is straightforward. In the case in which we have very little or no information about the driver source impedance, we need to measure two sets of s_{11} microwave scattering parameters looking into the driver output, using a microwave vector network analyzer such as the HP 8510. For both sets, the driver output bias level is set to the value to be used in practice. In the first set, we have the output modulation current (which is added to the bias current) set to zero, and in the second set, we have the output modulation current at the high value as used in practice. We can fit two equivalent circuits to the two sets of s-parameters. Finally, we merge the two circuit topologies to end up with one description for the source impedance of the driver.

From inspection of a Smith chart plot of s_{11}, one can tell whether the driver circuit is based on silicon bipolar or GaAs FET technology because of the telltale dispersion in the output conductance of GaAs FETs. In this example, we have fitted the equivalent circuit shown in **Figure 2** to describe the source impedance of a GaAs FET-based laser diode driver. The parallel RC (PRC) combination models the nonzero output conductance (finite output resistance) of the output transistors in the driver and the output capacitance of the transistors. The series RC (SRC) circuit combination describes the dispersion in the output conductance of the GaAs FETs as a function of frequency. The inductance (IND) models the bond wire from the chip to the carrier. The ideal transmission line (TLIN) models any transmission line between the measurement reference plane and the location of the bond wire. This last element is important since one often encounters s-parameter measurement data that has not been completely deembedded.

Figure 2

Equivalent circuit developed to describe the source impedance of a GaAs FET-based laser diode driver.
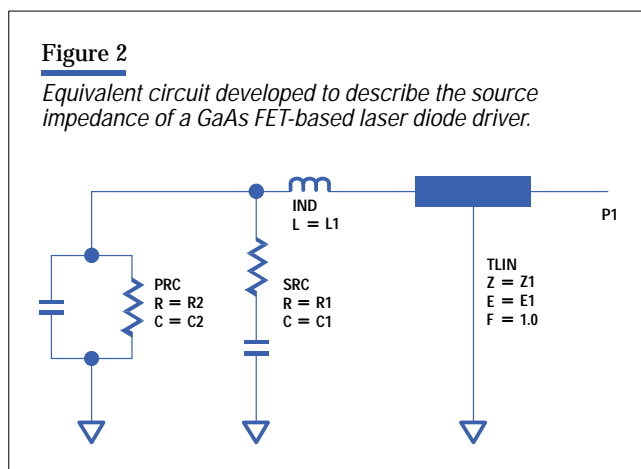
Using a small-signal microwave circuit simulator with optimization capability, one can find the best set of parameters for the circuit elements that gives the best agreement between the measured s_{11} data and the s_{11} values predicted by the circuit simulator. Typical values for the circuit of Figure 2 for a GaAs FET-based driver, derived through the use of linear circuit optimization, are as follows: R2 = 349Ω, R1 = 216Ω, L1 = 0.757 nH, C2 = 1.45 pF, C1 = 15.0 pF, Z1 = 139Ω, E1 = 7.09 degrees.

The inverse of the R1·C1 product defines the frequency in radians at which the output resistance of the transistor changes from being R2 to being equal to the parallel combination of R1 and R2. In this example, this break frequency is just above 49 MHz. At frequencies well below 49 MHz, the output resistance is 349 ohms (R2), whereas at frequencies well above

49 MHz, the output resistance of the source FETs is about 133 ohms. This change in output resistance of the driver transistors is referred to as the dispersion in the transistor output conductance (or resistance). The value of 7.09 degrees at 1.0 GHz for the TLIN indicates that there was some residual transmission line length that had not been removed during the microwave s-parameter measurement procedure.

In practice, the transistor can be considered to consist of a current source in parallel with the PRC circuit element in **Figure 2**. We can use either a large-signal, time-domain circuit simulator or a small-signal, frequency-domain circuit simulator to predict the shape of the driver output waveform. The manner in which a time-domain circuit simulator can be used is relatively straightforward, so we will illustrate the use of a frequency-domain circuit simulator. If we use a standard 50-ohm characteristic impedance to predict the s-parameters for the driver circuit, we can replace the current source in parallel with R2 by a voltage source in series with R2. The reason for replacing the current source with a voltage source is that the s-parameters are voltage ratio parameters, so we must use a voltage source. Since we use the standard 50-ohm resistance in series with the voltage source, we need only have $(R2-50)$ ohms of series resistance.

We can define a driving PRBS waveform for the voltage source and use the FFT algorithm to transform the time-domain representation of the waveform into the frequency domain. We can use a linear microwave simulator to predict the real and imaginary parts of the voltage transfer ratio s_{21} and convolve the predicted s_{21} response with the frequency-domain representation of the voltage source waveform. Finally, we use the inverse FFT to transform the frequency-domain representation of the output pulse back into the time domain. We know from measurements using an HP 54120B sampling oscilloscope that the 10%-to-90% rise and fall time for the pulse from the driver circuit is 130 ps. Consequently, we can engineer the rise and fall time of the voltage source pulse such that the pulse obtained from the driver circuit model corresponds to that measured from the real driver circuit.

Figure 3 shows the driver circuit model obtained in this way along with the voltage source waveform and the driver circuit model output waveform.The waveform time axis extends from zero to 3.2 ns. The 10%-to-90% rise and fall time for the voltage source signal connected in series with a 50-ohm resistance to port 1 is 75 ps as generated by the PRBS test set. The model predicts a rise and fall time for the waveform from port 2 of 127 ps, which corresponds well with a measured value of around 130 ps.

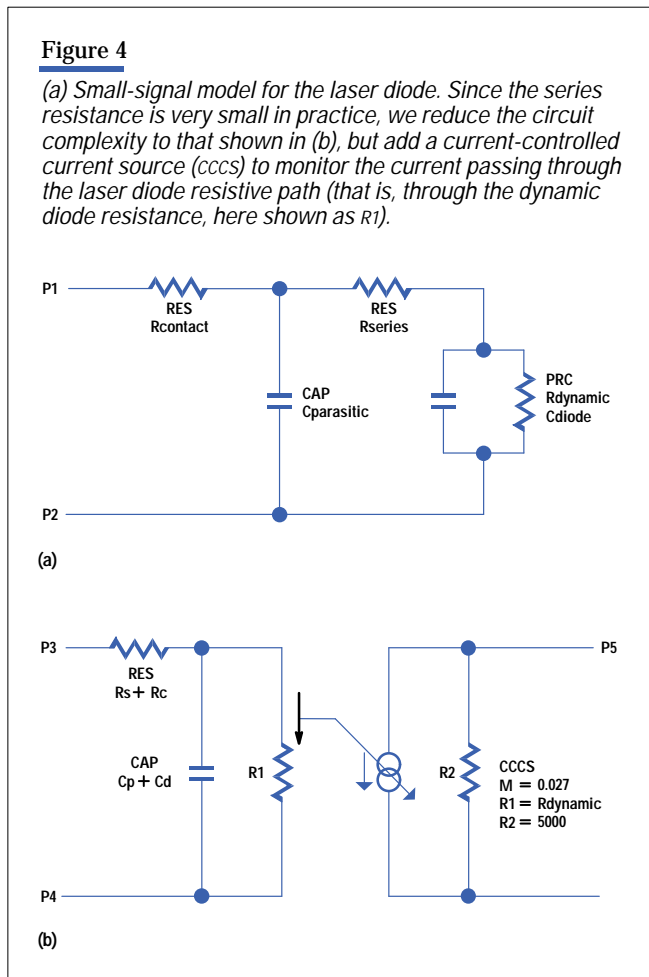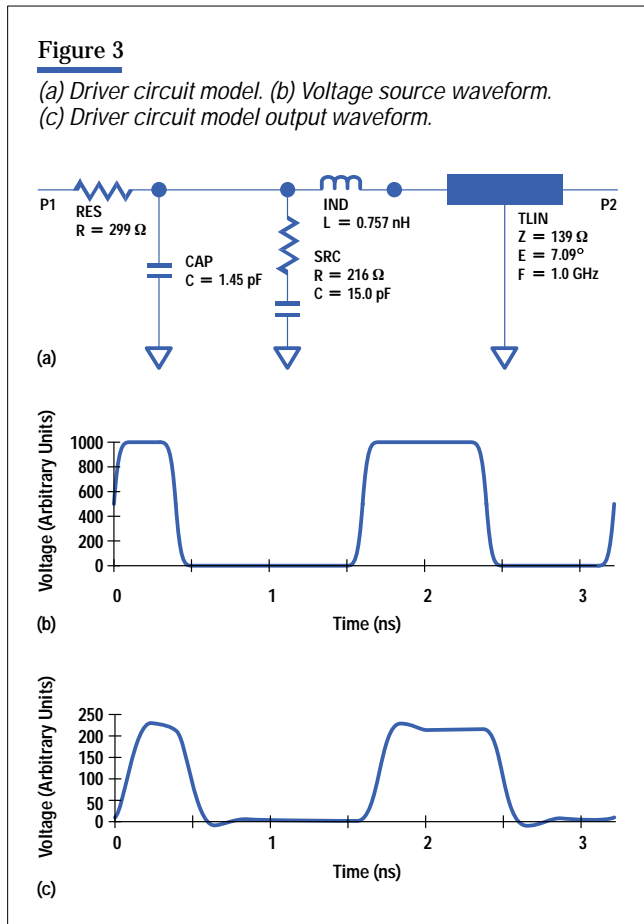### Electrical Model for the Laser Diode

The next task is to create an electrical model for the distributed feedback laser diode. We first look at the construction of a model for use with a linear circuit simulator. From the S-shaped I-V characteristics of the laser diode, we find that in a manner analogous to that used in the Gummel-Poon model for the silicon bipolar transistor, we can simulate the dc I-V characteristics through the use of a resistance in series with two parallel diodes. We have written parameter extraction software for such a combination of diodes to find the parameters that best fit the classical exponential diode equation:

$$I = I_s\left(e^{aV/nkT} - 1\right).$$

In this example we found that the best-fit parameters are $I_{s1} = 1.1 \times 10^{-6}$ amperes and $n_1 = 3.9$ for the first diode, $I_{s2} = 1.0 \times 10^{-13}$ amperes and $n_2 = 1.18$ for the second diode, and $R_{series} = 5.5$ ohms.

Diode 1, with $n_1 = 3.9$, dominates the diode characteristics for forward currents through the laser diode of less than 1 mA, whereas diode 2 dominates the characteristics at 1 mA and above. Since the laser diode is always biased in the on state with about 15 mA of current, we consider only the characteristics of diode 2. With the electrical characteristics of the DFB laser diode following the classical exponential diode equation, we calculate a dynamic laser diode resistance of 7.5 ohms when biased at 15 mA (the zero state close to threshold) and 6.2 ohms when biased at 45 mA (the one state). Since the laser diode will spend about the same time in the zero state as it does in the one state, we take the arithmetic mean of the dynamic resistances to end up with 6.85 ohms.

In all modeling of physical devices, it is important to keep in mind the physics of the device being modeled. The small-signal model for the laser diode is shown in **Figure 4a**. Since the series resistance is very small in practice, we reduce

Figure 3

(a) Driver circuit model. (b) Voltage source waveform. (c) Driver circuit model output waveform.

(a)

(b)

(c)

Figure 4

(a) Small-signal model for the laser diode. Since the series resistance is very small in practice, we reduce the circuit complexity to that shown in (b), but add a current-controlled current source (cccs) to monitor the current passing through the laser diode resistive path (that is, through the dynamic diode resistance, here shown as R1).

(a)

(b)

the circuit complexity to that shown in **Figure 4b**, but add a current-controlled current source (CCCS) to monitor the current passing through the laser diode resistive path (that is, through the dynamic diode resistance, here shown as R1). The current amplification factor M is negative to enable us to monitor the magnitude of the current passing through the dynamic resistance. To get the voltage generated by the CCCS across the 50.0 ohms at the output port of the CCCS to equal the voltage across the dynamic resistance (Rdynamic), we must have the magnitude of the CCCS current amplification factor equal to Rdynamic/ 50.0, that is, 0.027. We used the HP 8702 vector network analyzer connected to a PC via an HP-IB (IEEE 488, IEC 625) link to derive the electrical s-parameters (i.e., s_{11}) for the laser diode, and we used the HP VEE software to save the data as an industry-standard S1P one-port s-parameter device file. We then used the optimization feature in the linear circuit simulator to derive the best-fit resistance and capacitance values.

Package Model

The standard specifications for the package call for a standard impedance level of 25 ohms. The approach taken by HP is to use a submodule containing the laser diode, a chip resistance used for wide-bandwidth impedance matching, and some other optical components. This submodule is mounted on a thermoelectric cooler inside the overall industry-standard butterfly package, which also contains another chip resistor, a chip capacitor, and a chip inductor. To model the electrical response of the packages and the components within the packages accurately, we made extensive use of a vector network analyzer to derive the best equivalent circuit topologies and the best values for the elements within the

equivalent circuit for the chip resistors, chip capacitor and chip inductor. The model for the chip inductance was by far the most complex, but a multisection, finite-Q (quality factor) circuit topology enabled us to predict all the measured resonances.

Additionally, we made a careful analysis of the bond wire lengths. In this analysis, we use Bezier curves to simulate the side views of the bond wires, from which we can quite accurately predict bond wire length. Remember that even at 2 GHz, a 1-mm bond wire will have an inductive reactance of about 12.6 ohms, which is significant in a 25-ohm characteristic impedance system. Therefore, attention to detail was most important, and bond wire engineering played an important role in this design. An example of this work, taken from a different example, is as shown in **Figure 5**. In this work, we have looked at the use of ball and wedge bonding to get the best performance, while keeping the costs associated with high-volume manufacturing under control.

Figure 5

Package and circuit model for bond wire analysis.
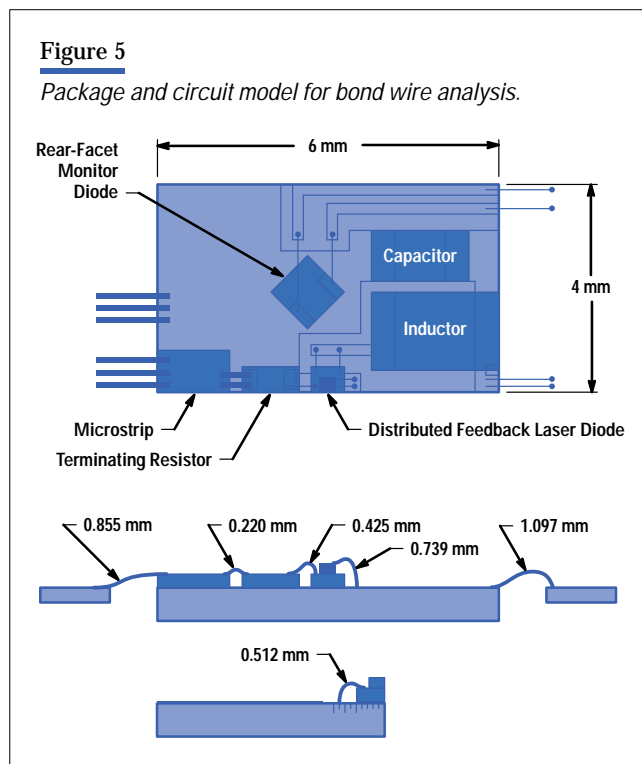
In our development work, we came to appreciate the value of the interaction between the simulation work and the precision measurements that were made on the devices and circuits. Several special test fixtures were constructed for use in the measurement of the characteristics of the laser diode. These precision fixtures were intended for use up to 6 GHz and have standard SMA connectors. We carefully characterized the fixtures so that any component or circuit could simply be placed within the test fixture environment as a subcircuit, simplifying the extraction of the parameters for the elements within the subcircuit. We used standard optimization techniques to get the equivalent circuit response to match the measured response. It is necessary to minimize the number of optimization variables because the difficulty of finding the global minimum using an optimizer increases rapidly as the number of variables increases.

The circuit topology for the overall package is too detailed for us to describe at any length in this paper. We export the predicted s-parameter response for the circuit to a standard S2P s-parameter file. In a 50-ohm characteristic impedance system, we predict the s_{21} response as shown in **Figure 6a**, together with the group delay shown in **Figure 6b**. The input reference plane (port 1) is at the end of a microstrip line on a printed circuit board substrate 8.0 mm from the butterfly

package itself. The bias and the signal are brought in through separate terminals on the butterfly package. The group delay plot is important since we need to maintain the integrity of the rectangular pulses coming in, pulses with Fourier components that we must be concerned with up to at least 2 GHz. The response shown in **Figure 6a** is what we would expect to measure using a vector network analyzer in a 50-ohm environment. In practice, a laser diode driver chip is used to supply the bias current and drive the pulses into the laser diode.

Figure 6

(a) Overall package model s_{21} response. (b) Package model group delay response.
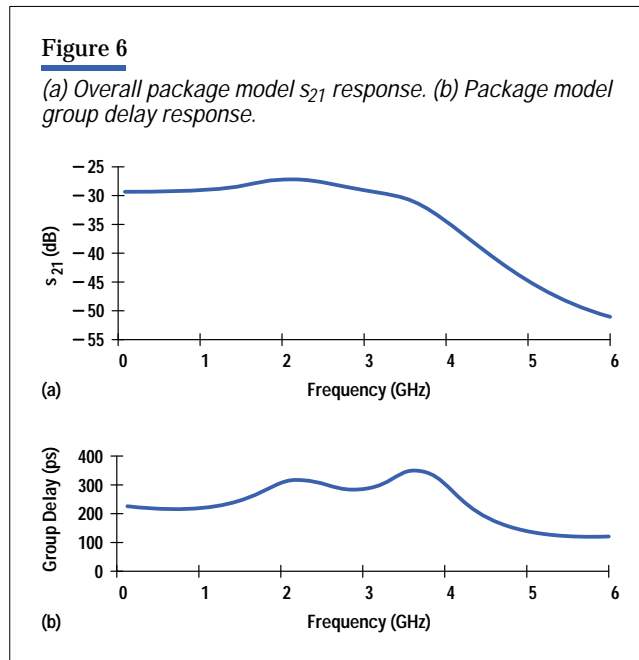
Having defined the package response in an s-parameter file, we can apply the FFT technique discussed earlier to the s_{21} voltage transfer ratio to predict the voltage across the laser diode dynamic resistance, and consequently, the current through the resistive part of the laser diode. This we have done for the case in which the packaged laser diode is driven directly from a 50-ohm characteristic impedance PRBS test set, and for the case in which the packaged laser diode is driven from the laser diode driver example discussed before. In **Figure 7**, the 2.488-Gbit/s voltage waveform with a 10%-to-90% rise and fall time of 75 ps from the signal generator is shown on top, and below it the predicted current waveform into the laser diode when the packaged laser diode is driven directly from the test set. The bottom waveform represents the case in which the laser diode driver is used. Note that the laser diode driver slows down the rising and falling edges of the waveform.

Using a fast sampling oscilloscope to monitor the current through the laser diode, we then predict the waveform display for the oscilloscope triggered at twice the bit interval to look as shown in **Figure 8**. The plot resembles the eye diagram frequently used in communications engineering. The upper plot is driven directly from the fast PRBS test set, while the lower plot is with the laser diode driver present. In both cases, we notice the effects of overshoot.

Before the predicted current waveform into the laser diode is used in the laser diode simulator to predict the amplitude and the wavelength of the light emitted from the laser diode, we rescale the amplitude of the predicted current and add the laser diode bias offset.

Laser Model

A laser model for multiple quantum well distributed feedback lasers has been developed specifically for dynamic laser modeling. Emphasis has been placed on developing fast simulations that can readily be used for design and optimization,

Figure 7

(a) 2.488-Gbit/s voltage waveform with a 10%-to-90% rise and fall time of 75 ps from the signal generator. (b) Predicted current waveform into the laser diode when the packaged laser diode is driven directly from the test set. (c) Predicted current waveform into the laser diode for the case in which the laser diode driver is used.
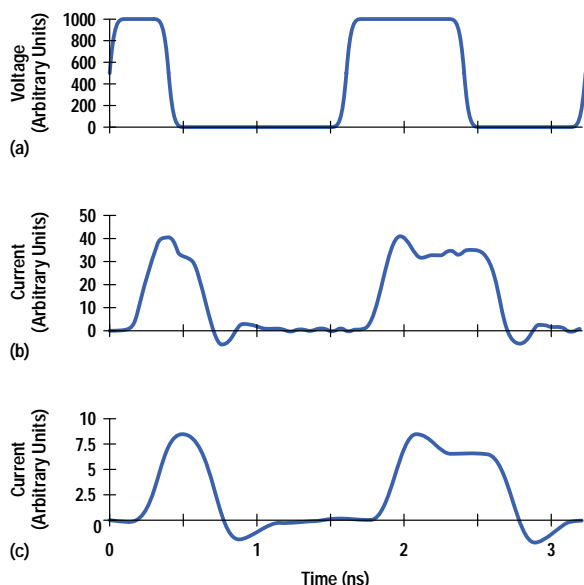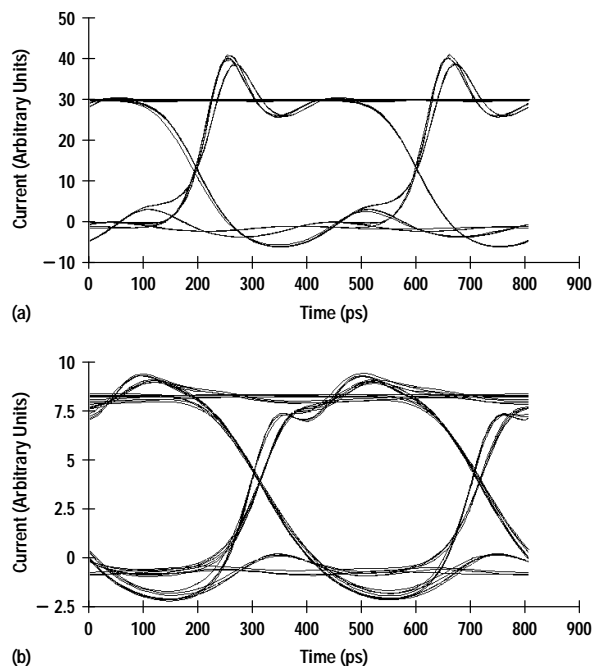

Figure 8

Waveforms of Figure 7 displayed on an oscilloscope triggered at twice the bit interval. The plots resemble the eye diagram frequently used in communications engineering. (a) Waveform of Figure 7b. (b) Waveform of Figure 7c.


and hence lumped spatial models have been used rather than traveling-wave models. By implementing empirical descriptions obtained from rigorous steady-state models, longitudinal-mode spatial hole burning in distributed feedback lasers could be included. Such descriptions also make it possible to take into account the effect of the coupling strength of the internal grating. To model the high levels of hole burning observed both in phase-shifted gratings and in antireflection and high-reflection coated lasers, the laser is subdivided into three sections along the cavity to account for the resulting inhomegeneity. The three sections are coupled to each other and the photon population through empirical relations which are derived from traveling wave models.

The model also includes nonlinear effects resulting from carrier transport in quantum well lasers through the implementation of a barrier-level carrier rate equation. The barrier carrier population is coupled to the well carrier population through capture and escape processes. These processes describe the carrier bottleneck, which can significantly reduce the laser bandwidth.

Of key importance in the carrier dynamics is the time taken for electrons to cross the separate confinement layers and to be captured by the wells. This limits the dynamic performance of high-speed lasers. While the capture process itself may occur on subpicosecond time scales, the diffusion across the confinement layers can take tens of picoseconds. This is shown schematically in **Figure 9**. The diffusion time constant depends on waveguide dimensions and doping levels. Thermionic emission of carriers back out of the wells into the barrier and waveguide layers also occurs, again on time scales of tens of picoseconds. This emission time constant can be controlled by varying the well and barrier dimensions. It is evident that a short diffusion time constant and a long emission time constant lead to efficient carrier injection

Figure 9

Diffusion across the confinement layers in a multiple quantum well distributed feedback laser. (SCH is the waveguide, or separate confinement heterostructure.)
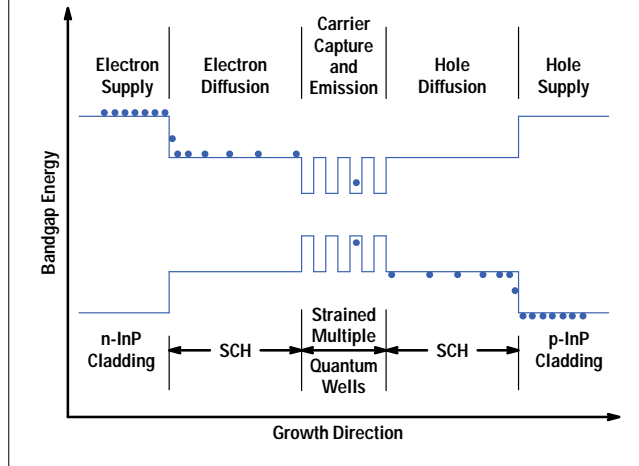
into the wells and enhanced bandwidth. Alternatively, careful design of the quantum wells suppresses unwanted high-frequency oscillations responsible for excess wavelength chirp and patterning under digital modulation. The electron rate equation for the barrier and confinement layers has therefore been introduced to account for carrier injection initially into the barrier levels, and to describe the coupling between carriers in the barriers and the wells:

$$\frac{dN_b}{dt} = \frac{J}{qd_b} + \frac{N_w}{\tau_e}\frac{V_w}{V_b} - \frac{N_b}{\tau_c}.$$

Here N_b and N_w represent the carrier densities in the barriers and wells, respectively. V_b and V_w are the volumes in the barriers and wells. d_b accounts for the depth of the separate confinement layers. The current density J is injected into the separate confinement layers. q is the electron charge. The carriers are depleted with a capture lifetime τ_c. This lifetime is dominated by the diffusion across the layers and is of the order of tens of picoseconds. Carriers are also reinjected from the wells into the barrier and confinement layers with an associated time constant τ_e, which is determined by the thermionic emission. This can be of the order of a hundred picoseconds, and has significant temperature dependence.

The injection of carriers into the quantum well is therefore determined by the ratio of the diffusion and capture rate time constant to the thermionic emission rate. This creates a carrier bottleneck of considerable importance for high-bandwidth lasers. The rate equation for carriers in the wells is therefore written in terms of the capture and emission rates:

$$\frac{dN_w}{dt} = \frac{N_b}{\tau_c}\frac{V_b}{V_w} - \frac{N_w}{\tau_e} - v_gGP - \frac{N_w}{\tau_s}.$$

The above equation also takes into account carrier depletion through stimulated emission, which is described by the term v_gGP, where v_g is the group velocity of light in the laser cavity, G is the optical gain, and P is the photon density. Both radiative and nonradiative recombination mechanisms are described through the carrier lifetime τ_s. The gain term includes a linear dependence on the carrier density and a nonlinear gain compression term ε:

$$G = \frac{(dg/dN)(N_w - N_t)}{(1 + \varepsilon P)},$$

where dg/dN is the differential gain and N_t is the transparency carrier density. In the simulation, the parameters used in the modeling have been derived from steady-state measurements wherever feasible. The gain has been modeled by assuming a linear differential gain dg/dN of 6×10^{-16} cm^2, a transparency carrier density N_t of 1.5×10^{18} cm^{-3}, and a gain suppression factor ε of 3×10^{17} cm^3. The gain suppression factor accounts for nonlinearities such as spectral hole burning, carrier heating, and transverse-mode spatial hole burning.

The rate equation for the photons is coupled only to the carrier population in the wells:

$$\frac{dP}{dt} = \Gamma\beta B N_w^2 + \Gamma v_g G P - \frac{P}{\tau_p}.$$

The term $v_g G P$, which depletes carriers in the wells (N_w), feeds photons into the guided laser beam. The spontaneous emission is described by the term $\Gamma\beta B N_w^2$, where Γ describes the overlap of the optical mode with the quantum wells, β is the spontaneous emission coupling factor, and B is the bimolecular recombination coefficient. τ_p is the photon lifetime, which is a function of the grating coupling strength.

The cavity refractive index is perturbed by fluctuations in the carrier density to chirp the operating wavelength λ. Because wavelength chirp limits device performance as described earlier, the linewidth enhancement factor α_H is introduced to describe chirp for a given laser structure. The linewidth enhancement factor is proportional to the quotient of the differential refractive index dependence on carrier density $d\mu/dN$ and the differential gain dg/dN.

$$\alpha_H = \frac{4\pi}{\lambda}\frac{d\mu/dN}{dg/dN}.$$

The lower the value of α_H the lower the wavelength chirp. The linewidth enhancement factor for a strained quantum well InGaAsP laser is approximately 2.5.

The transport effects lead to a significant carrier population in the barriers and the confinement layers. Because a significantly larger proportion of the optical mode overlaps with the confinement layers when compared with the wells, this population also perturbs the effective refractive index of the cavity and therefore leads to enhanced wavelength chirp. The overall effective refractive index perturbation can therefore be summarized in terms of contributions from the barriers and the wells:

$$\mu_{eff} = \Gamma_w\frac{d\mu}{dN_w}N_w + \Gamma_b\frac{d\mu}{dN_b}N_b.$$

The rate equations are solved using Runge-Kutta algorithms.

The laser model is written using C++ and runs on a PC and is fast enough to be suitable for interactive use. The outputs are described in terms of the time-resolved power and wavelength.

Optical Fiber Model

This model takes the complex optical field generated by the laser model to determine the signal propagating along the fiber. The optical field experiences a frequency dependent retardation as it propagates along the fiber. The model accounts for dispersion using the transfer function H(f):

$$H(f) = \exp\left(-j\frac{\pi D\lambda^2 L}{c}f^2\right).$$

In the simulation, D is the fiber chromatic dispersion, λ is the center wavelength, L is the fiber length, f is the baseband frequency, and c is the speed of light. The dispersion D is assumed to be 17 ps$\cdot$nm^{-1}km^{-1}. The model assumes that first-order dispersion dominates and neglects nonlinearities, a justifiable assumption for low-power radiation (<10 dBm) at 1550 nm in standard-dispersion fiber. The output optical pulse after any desired length of fiber can be predicted.

The fiber output power is incident on a square-law detector, the output of which is subsequently filtered in the frequency domain by a fifth-order Bessel filter with a bandwidth of 0.7 times the bit rate. Superposition of bit periods gives eye diagrams, which can be compared directly with experiment.

A schematic drawing of the elements of the laser and fiber model is shown in **Figure 10**.

Figure 10

Laser and fiber model.
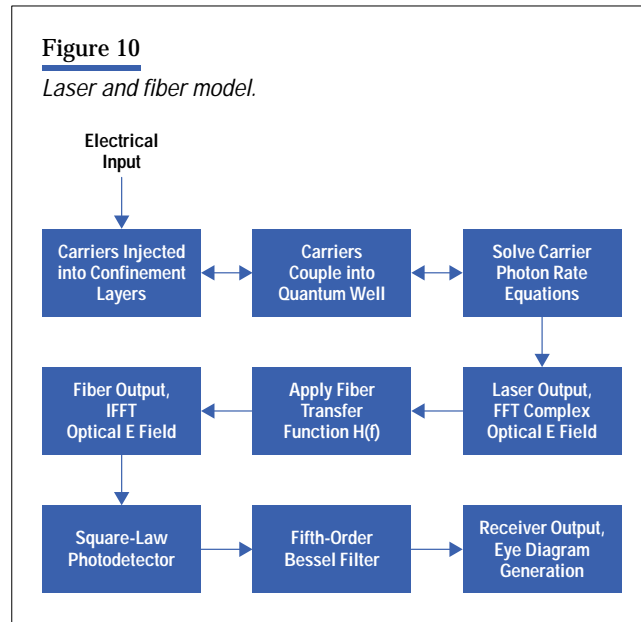
Comparison of s-Parameter Results

This section presents a comparison of the modeled and measured s_{11} and s_{21} parameters for an HP LSC2500 2.488-Gbit/s DFB laser diode developed at ICO. The s_{11} measurement determines the reflected power from the 25Ω-terminated laser diode into the 50Ω HP 85047A s-parameter test set. The s_{21} measurement determines the AM response of the laser diode. This is measured at high bias currents (where the intrinsic relaxation resonance of the chip is out of the frequency band of interest) to compare the measured result with the purely electrical microwave model.

Using WaveMaker software, a complete circuit description of the modulation signal path, from the RF pin on the butterfly package through the laser diode and back out to the two ground pins of the outer package, was constructed in a netlist format. Electrically, the laser diode was modeled as a 7Ω resistor (determined by experimental measurement) in parallel with a 4-pF capacitor (estimated from the structural layout).

s_{11} **Measurements.** The netlist was written to display the modeled and measured s_{11} results on the same plot. The circuit element values can then be adjusted, maintaining realistic values, to best match the measured data over the frequency range of interest.

The model was used to determine the effect of changing component values on the s-parameter response. This strategy was used to determine component values that will optimize the product performance and to set tolerances on component values and bond wire lengths.

s_{21} **Measurements.** The s_{21} measurement is an electrooptical measurement that cannot be truly accounted for in Wave-Maker because of the relaxation oscillation of the laser chip. However, by using a high drive current for the laser diode to

push any intrinsic resonance effects of the laser diode well out of the 6-GHz bandwidth of interest, it is possible to compare the modeled and measured data. This purely electrical model then predicts the measured s_{21} parameter except in magnitude, since no account can be taken of the laser diode's electrooptic conversion efficiency.

The simulation results in **Figure 11** and **Figure 12** show the best achieved s_{11} and s_{21} fits, respectively, for a 2.488-Gbit/s DFB laser that has an impedance matching resistor and a 3.9-pF capacitor in the package. The capacitor is placed in parallel with the laser diode, thereby establishing a resonant circuit between the capacitor, the resistance of the laser chip, and the inductance of the gold wire bonds. The response of the resonant circuit smooths out the rising edge of the electrical pulse, preventing overshoot and hence minimizing wavelength chirp.

Figure 11

A plot comparing the measured and modeled s_{11} parameters.
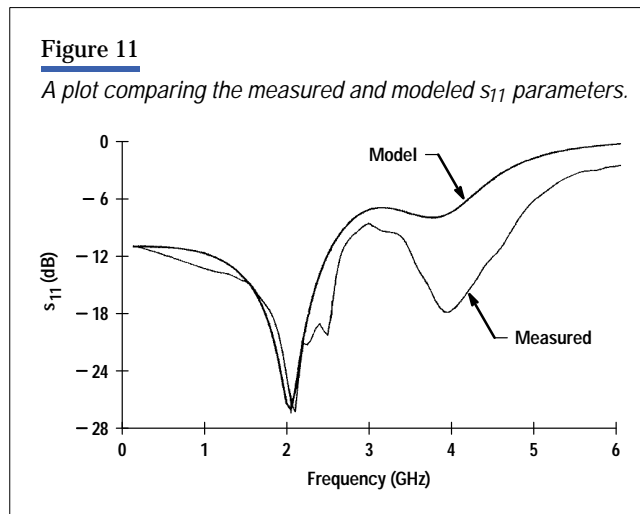
The bond wires in the package were modeled as pure inductances using the well-established value of 1 nH of inductance per millimeter of bond wire for 17-μm-diameter bond wire. All of the connections on the RF path were made using two bond wires in parallel, which effectively halves the inductance value. For example, 0.7 nH represents two bond wires 1.4 mm long. It was found experimentally that additional bond wires do not reduce the inductance significantly more because of the inevitable closer proximity of these wires on the bond pads.

Comparison of Measured and Modeled s_{11}. **Figure 11** shows a plot of the measured and modeled s_{11} parameters overlaid. The low-frequency (<3 GHz) fit of the model is quite respectable. It predicts the resonance resulting from the transition between the 50-ohm transmission line of the test set and the 25-ohm microstrip lines of the package to within 0.1 GHz and it also predicts the magnitude of the measured data generally to within better than 3 dB.

The resonance at 3.9 GHz caused by the interaction between the bond wire inductance, the capacitor, and the chip resistance is also predicted to within 0.2 GHz. However the depth of this resonance, or the Q factor of the oscillation, is not so well-simulated. The reason for this is not fully understood.

A feature of the measured results in **Figure 11** is sharp spikes in the s_{11} response at around 2.4 GHz. These have been found to be a resonance that occurs because the submodule base is not a true ground.

Figure 13 shows s_{11} measurements on ten different modules, showing the reproducibility. Variations in the 3.9-GHz resonance are attributed to tolerance variations in the capacitor used and bond wire length process variations. All of these measured results meet the s_{11} requirement for a 2.488-Gbit/s laser diode.

Comparison of Measured and Modeled s_{21}. **Figure 12** is a plot displaying the measured and modeled s_{21} parameters of a device. The low-pass filtering action seen in the measured s_{21} response is also modeled in WaveMaker. This filtering prevents high-frequency electrical oscillations from reaching the chip, which would cause it to produce unwanted optical

Figure 12

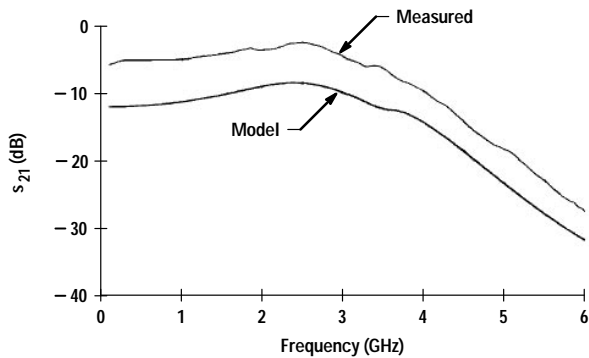A plot comparing the measured and modeled s_{21} parameters.

Figure 13

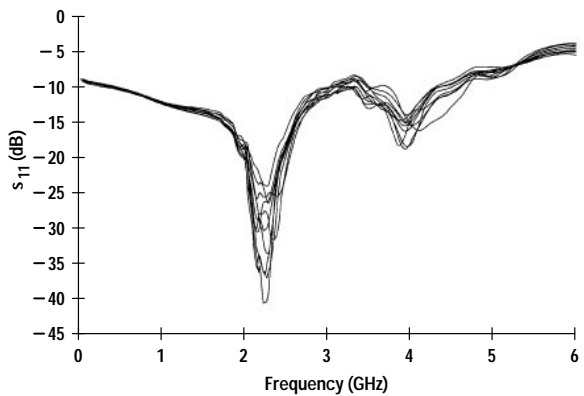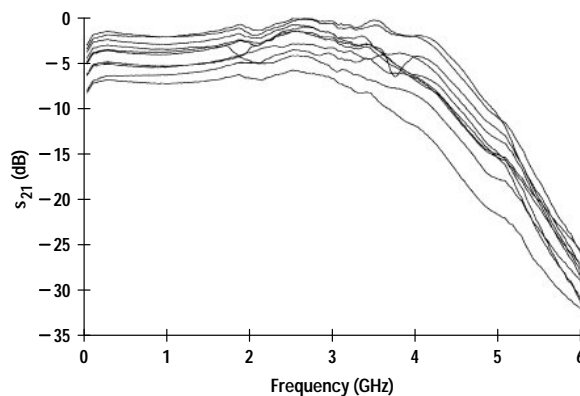A plot of s_{11} measurements on ten different modules.

Figure 14

A plot of s_{21} measurements on ten modules.

oscillations. Comparing the shapes of these curves, the modeled results predict 3.4 dB of ripple with a resonant peak at 2.4 GHz while the measured results show 2.6 dB of ripple with a resonance at 2.5 GHz. The roll-off of the modeled data is 9 dB/GHz, in good agreement with the measured data.

The 3-dB bandwidth requirement for a 2.488-Gbit/s laser is a 3.5-GHz minimum. The internal filter has been designed to give enough bandwidth and to limit the speed of the rising edge. **Figure 14** displays s_{21} measurements on ten modules, showing that typical modules have a 4-GHz 3-dB bandwidth.

Microwave Model Output. The modeled s_{21} parameter file is convolved with an ideal, user-defined pulse train in the frequency domain and then inverse Fast Fourier transformed back to give a realistic electrical pulse train in the time domain, which is then offset to set an extinction ratio. This offset electrical pulse can then be used as the input to a model developed by Bristol University, which takes an electrical current pulse input and, using parameters to describe

the laser diode in detail, models the optical output from the device. This model also includes a description of fiber parameters and can predict the optical pulses after lengths of fiber.

Comparison of Optical Pulse Shapes

The modeling software developed by the University of Bristol was designed to calculate the optical output of quantum well DFB laser diodes grown using the InGaAsP-InP material system. The model can be run using a time-domain description of an electrical pulse train as the input. This has been created at ICO using WaveMaker software, as discussed in the previous section. The Bristol software then models the laser's response to this large-signal modulation. The reason for installing these combined models at ICO was not only so that we could optimize the s-parameter response of the 2.5-Gbit/s laser but also so that we could predict the effects on the system performance of changing the package components and bond wire lengths by looking at the pulses at the receiver after the fiber. The unfiltered optical output can be displayed as pulses in the time domain before and after an arbitrary length of fiber, the dispersion properties of which can be specified.

The software also displays the wavelength deviation of the laser output during the pulse train, calculated from the known laser parameters. Depending on the timing of the wavelength deviation or chirp during a bit period, quite different effects can be seen when the signal is transmitted over fiber. At 1550 nm, short wavelengths travel faster through the fiber than long wavelengths. An optical pulse that starts with a short wavelength and ends with a long wavelength will spread apart over the fiber, while a long wavelength at the start and a short one at the end will cause the pulse to be compressed over the fiber.

This model has been used in conjunction with WaveMaker to model a system using an HP 2.5-Gbit/s directly modulated DFB laser in a 14-pin butterfly package as the transmitter, and over 106 km of standard single-mode fiber with 17 ps/nm/km of dispersion.

To test the accuracy of this combined model, the modeled results were compared with experimental results acquired by modulating the laser with an HP 70841B pattern generator. The output after the fiber was then fed into an HP 11982A lightwave converter with a 15-GHz bandwidth and the resulting pulses were displayed on an HP 54120B digital sampling oscilloscope. For this paper, a 0101 0011 pulse train was used to compare modeled with experimental results.

Back-to-Back (No Fiber) Results. **Figures 15a and 15b** show the comparison between modeled and experimental results measured back to back for a 2.5-Gbit/s laser. The pulse shape of single and double ones can be seen to be in good agreement with the measured data. It is important that the pulse widths for single and double ones are in both cases 400 ps and 800 ps, respectively.

The other features of the pulse train predicted by the model are the oscillations in both the double zeros and the double ones. The first oscillation in the double zero, caused by an electrical resonance between a 3.9-pF parallel plate capacitor, the bond wire inductance, and the laser resistance and capacitance, is predicted with correct magnitude. A second oscillation appears which is damped with respect to the first. The frequency of oscillation in the ones (again because of the electrical oscillations) is 2.5 GHz, in very good agreement.

Results over 106 km. Figures 16a and 16b display modeled and experimental data after transmitting the pulse through 106 km of fiber, equivalent to a dispersion of 1800 ps/nm at 1550 nm. As can be seen in both cases the pulses are getting narrower and the widths are still in reasonable agreement. It is the narrowing of the pulse width that has been found to cause an improvement in bit error rate over fiber. This can be explained by realizing that as the pulse compresses, the power at the decision point is raised, thus improving the signal-to-noise ratio at the receiver.

The features of the modeled pulses include the sharpening and subsequent buildup of optical power in the front of the pulses and the progression into the zeros of the small optical output that was induced by the resonance.

Figure 15

(a) Modeled 2.5-Gbit/s pulse train back to back.
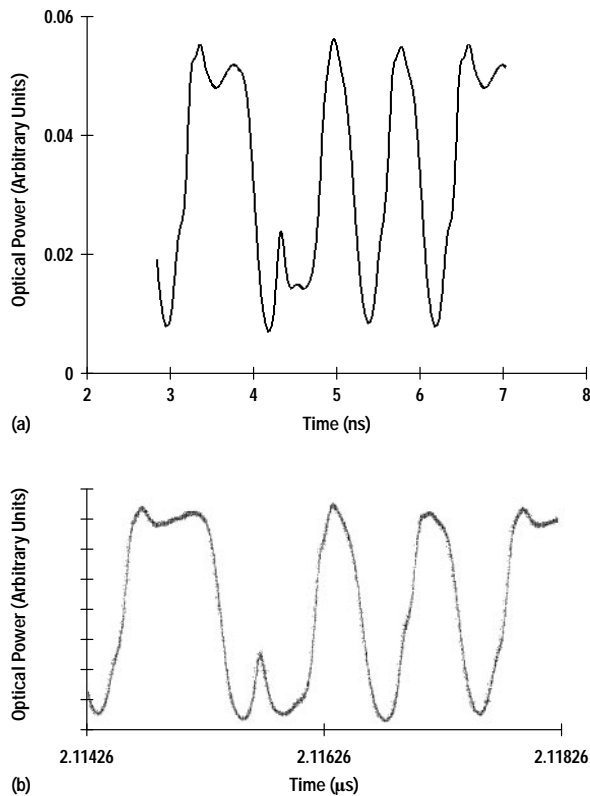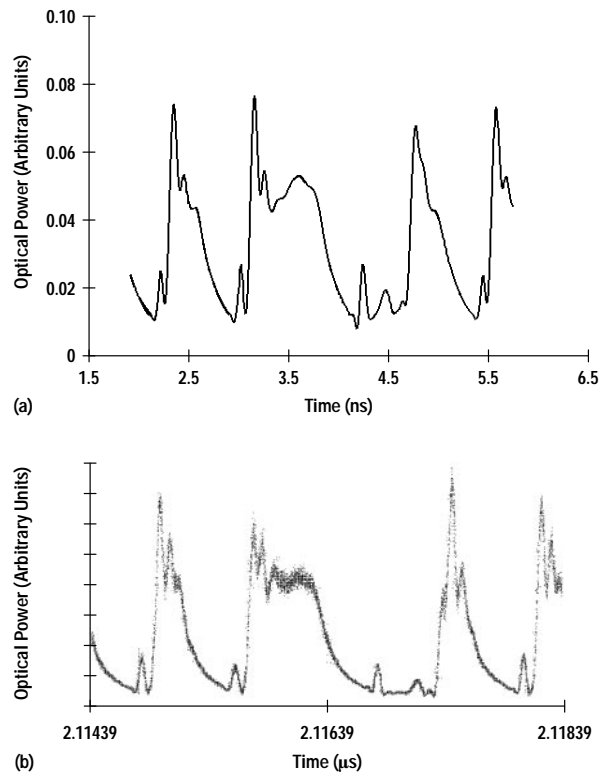(b) Measured 2.5-Gbit/s pulse train back to back.

(a)

(b)

Figure 16

(a) Modeled 2.5-Gbit/s pulse train after 106 km of fiber.
(b) Measured 2.5-Gbit/s pulse train after 106 km of fiber.

(a)

(b)

In summary, for both back-to-back transmission and transmission over 106 km of fiber, the model has predicted both pulse widths and pulse shapes with a reasonable degree of accuracy. The model was also successful in predicting specific features of the pulse train, such as oscillations and the sharpening of the rising edge.
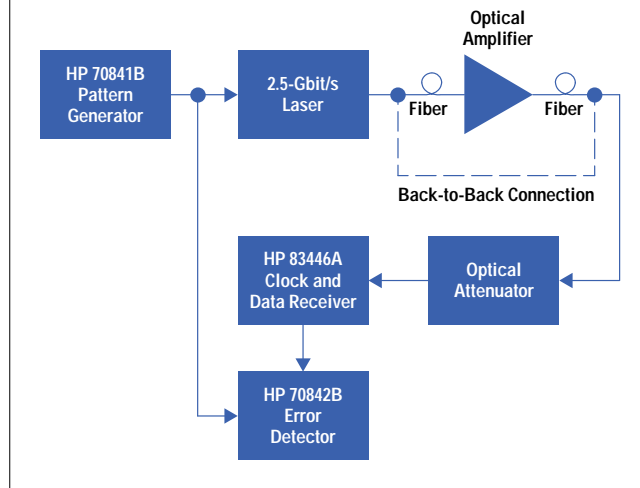
Dispersion Penalty Measurements

The combined models discussed in this paper were used to produce good s-parameter results and good pulse shapes over fiber. The experimental RF test to confirm this data transmission was the bit error rate test, the experimental arrangement of which is shown in **Figure 17**. A pseudorandom $2^{23} - 1$ bit stream is produced by the HP 70841B pattern generator at 2.488 Gbits/s. This data modulates the laser diode, which has a dc bias provided by a separate current source. The laser's optical output is then directed straight into an optical attenuator for back-to-back measurements or into the fiber, an amplifier (if required), and an attenuator for measurements over fiber. The purpose of the attenuator is to vary the power level reaching the receiver. The output of the attenuator is then fed into an HP 83446A STM 16 lightwave clock and data receiver, the output of which is fed into an HP 70842B error detector, which compares the transmitted and received optical pulses, measures the total number of erroneous bits received during a time period, and calculates the bit error rate.

Bit error rate curves are plotted in **Figure 18**. These are plots of bit error rate versus received power in dBm for varying extinction ratios, measured back to back and over fiber. As the power at the receiver increases, the bit error rate drops. The dispersion penalty indicates how much the power at the receiver must change to maintain the same bit error rate for

Figure 17

Schematic drawing of the bit error rate test setup.

measurements back to back and over fiber. The dispersion penalty can be seen as the horizontal displacement between the two bit error rate curves and is measured in dB. The value can be positive or negative as explained later.
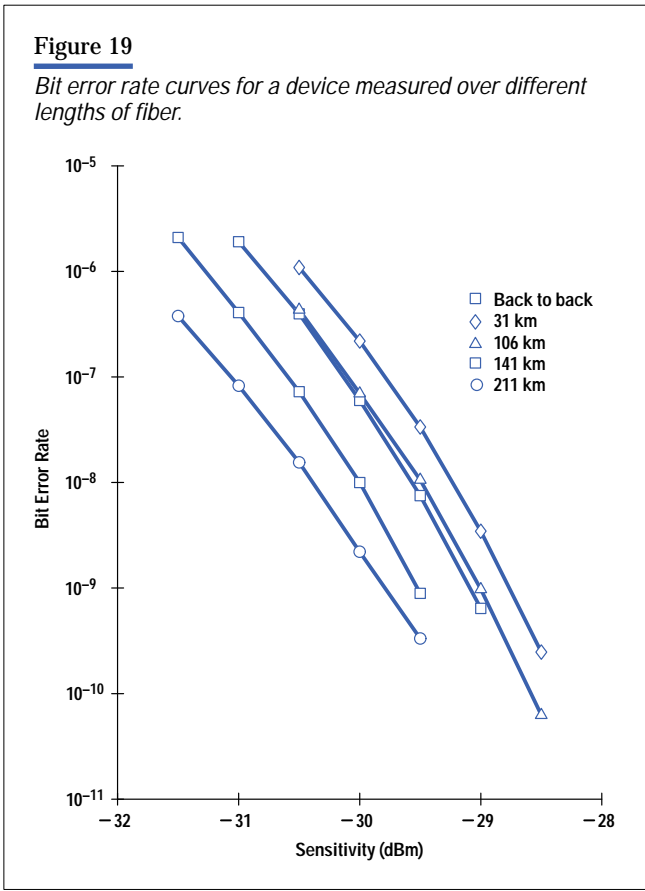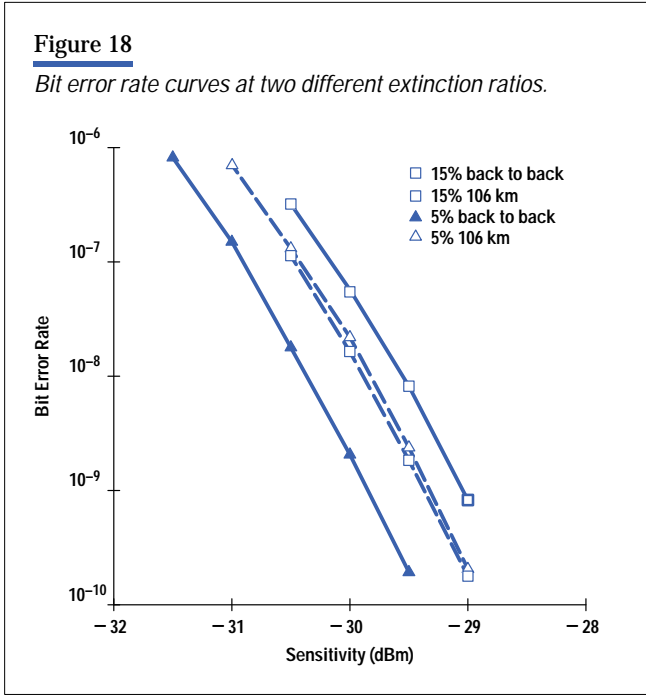
Figure 18 shows how these dispersion penalties depend on another parameter—the extinction ratio. The extinction ratio is a measure of how close to its threshold current or off state the laser is modulated. It is in the region closest to the threshold current that the largest changes in the device's carrier density, refractive index, and hence emission wavelength occur. To transmit data over fiber we intuitively want the wavelength to vary as little as possible between the on and off states. The extinction ratio is defined as the power in the off state divided by the power in the on state. The greater the extinction ratio the less the wavelength shift, but for maximum sensitivity it is desirable to have as little power as possible in the off state. A compromise value must be used. The measurements in Figure 18 were taken at extinction ratios of 5% and 15%. The respective dispersion penalty measurements over 106 km of fiber are 0.5 dB and −0.33 dB.

Figure 19 shows bit error rate results for a device measured back to back, at 530 ps/nm (31 km), 1800 ps/nm (106 km), 2400 ps/nm (141 km), and 3600 ps/nm (211 km). Here it can clearly be seen that the dispersion penalty can improve over fiber. The improvement in the dispersion penalty is attributed to the pulse compression that takes place over the fiber when pulses consist of long wavelengths at the beginning and short wavelengths at the end. Over 211 km, a double pulse compresses from 800 ps to 624 ps, which must be close to the limit of useful compression if the sampling is halfway through each bit.

In this example, the error rate is seen to get worse over shorter distances of fiber before improving over longer distances. This can be explained by power leaving the center of the pulse before being replaced by the faster traveling tail. This confirms that it is not only the magnitude of the chirp but also the timing of it that is important.

Conclusion

We have described the microwave, laser, and fiber models that were used in the development of the HP LSC2500 2.488-Gbit/s DFB laser diode module. These models have been shown to accurately predict the microwave s-parameters of the laser module and therefore the electrical signal reaching the laser diode. Knowing the electrical signal to the laser, the optical output has been predicted, which leads to the wavelength chirp and therefore the dispersion penalty over long lengths of single-mode fiber at 1550 nm. The predicted optical pulse shapes both before and after the fiber agree closely with the experimental results.

Figure 18

Bit error rate curves at two different extinction ratios.

Figure 19

Bit error rate curves for a device measured over different lengths of fiber.

With the aid of the models, a low-chirp multiple quantum well DFB laser module has been developed. Knowledge of the modeled behavior of the laser diode as a function of the input electrical pulse shape has led to deliberately shaping the input pulse to give the minimum wavelength excursion during direct modulation, and therefore a high yield of low-dispersion-penalty laser diodes. We have also demonstrated that these devices can be successfully used for transmission distances in excess of 200 km.

Acknowledgments

Stephen M. Gee
Steve Gee is a senior engineer at HP's Ipswich, England Components Operation. He is currently part of the team working on a 2.5-Gbit/s electroabsorption modulator and a 2.5-Gbit/s transceiver. He joined ICO in 1995 after receiving his BSc degree in physics and physical electronics from the University of Bath. His nonwork interests include playing football and cricket and cycling.

Herbert Lage
Herbert Lage is a device engineer at HP's Ipswich Components Operation (ICO), where he is working on the development of distributed feedback laser chips. A native of Dortmund, Germany, he received a doctorate in physics in 1992 and worked as a senior scientist at Tele Danmark Research before joining ICO in 1994. He enjoys skiing, windsurfing, and tennis in his nonwork time.

Chris Park
Chris Park is a program manager at HP's Ipswich, England Components Operation. He is currently focusing on a wavelength division multiplexed version of the HP LSC2500 optically isolated distributed feedback laser module and on a 2.5-Gbit/s transceiver. A native of Halifax, Yorkshire, England, he is married and has three children.

Kevin A. Williams
Kevin A. Williams is a Royal Society University Research Fellow at the University of Bristol (United Kingdom), where he teaches in the Department of Electrical and Electronic Engineering. Kevin received his doctorate in physics in 1995 from the University of Bath.

Richard V. Penty
Richard V. Penty is a Lecturer in electronic engineering at the University of Bristol (United Kingdom). He received a doctorate from Cambridge University in 1990, specializing in nonlinear optical fibers. A native of Nottingham, England, he is married and the father of two children.

Ian H. White
Ian H. White is Professor of optical communications systems at the University of Bristol (United Kingdom). He teaches in the Department of Electrical and Electronic Engineering. Professor White received his doctorate in electrical sciences from Cambridge University in 1984.

Joseph A. Barnard
Joseph A. Barnard is managing director of Barnard Microsystems Limited in London, England. His expertise is in microwave optoelectronic circuit and system design software, and he has published widely on different aspects of this subject. He received a doctorate in engineering physics in 1982 from Cornell University. He is an avid tennis and chess player.